ACS Energy Letters

Cite This: ACS Energy Lett. 2018, 3, 1373−1380

Nickel Vacancies Boost Reconstruction in Nickel Hydroxide Electrocatalyst

Qun He,[†,§] Yangyang Wan,[‡,§] Hongliang Jiang,[*,†] Ziwen Pan,[∥] Chuanqiang Wu,[†] Mei Wang,[∥] Xiaojun Wu,[*,‡] Bangjiao Ye,[∥] Pulickel M. Ajayan,[#] and Li Song[*,†]

[†]National Synchrotron Radiation Laboratory, CAS Center for Excellence in Nanoscience, University of Science and Technology of China, Hefei 230029, PR China

[‡]Hefei National Laboratory for Physical Science at the Microscale, Synergetic Innovation of Quantum Information & Quantum Technology, School of Chemistry and Materials Sciences, and CAS Center for Excellence in Nanoscience, University of Science and Technology of China, Hefei, Anhui 230026, PR China

[∥]State Key Laboratory of Particle Detection and Electronics, Department of Modern Physics, University of Science and Technology of China, Hefei, Anhui 230026, PR China

[#]Department of Materials Science and NanoEngineering, Rice University, Houston, Texas 77005, United States

Supporting Information

ABSTRACT: **Because the reconstruction of catalysts is generally observed during oxidation reactions, understanding the intrinsic structure-related reconstruction ability of electrocatalysts is highly desirable but challenging. Herein, a controllable hydrolysis strategy is developed to obtain nickel hydroxide electrocatalysts with controllable nickel vacancy (V_{Ni}) concentrations, as confirmed by advanced spectroscopic characterization. Electrochemical measurements show that the reconstruction can be promoted with the increase of V_{Ni} concentration to generate true active components, thereby boosting activities for both oxygen evolution reaction (OER) and urea oxidation reaction (UOR). Density functional theory calculations confirm that the increased V_{Ni} concentration yields decreased formation energies of the true active components during reactions. This work provides fundamental understanding of the reconstruction ability of electrocatalysts in anodic oxidation reactions from the view of intrinsic defects.**

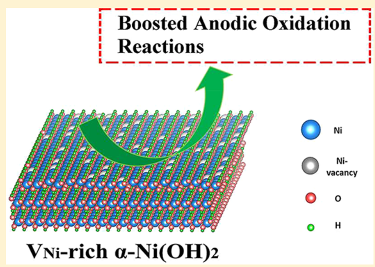

Developing feasible strategies, such as water splitting and fuel cells, to mitigate energy and environmental issues has become a focus of world attention.[1−3] In these devices, two typical anodic oxidation reactions, oxygen evolution reaction (OER) and urea oxidation reaction (UOR), have received considerable research and development attention because of their sluggish reaction kinetics.[4−10] Developing highly efficient electrocatalysts is the key to accelerating the reaction kinetics. In this regard, transition metal-based (Ni, Fe, Mn, Co, etc.) compounds have recently been considered as promising alternatives because of their earth-abundant and tunable properties.[11−15] For these catalysts, tuning their atomic and electronic structures has been proven to be an efficient method to optimize the catalytic performance.[12−15] Moreover, understanding the correlation between intrinsic structure and catalytic performance is of great importance to reveal the catalytic mechanisms. Among methods for structural regulation, atomic defect engineering, especially vacancy defect introduction, has been considered as an efficient approach to regulate the atomic and electronic structures of catalysts.[16−22] At this point, the defect types and concentrations are the main subjects of variation. For example, some effects have shown that the defective structure could enhance the activities of oxidation catalysts because of the exposure of a great number of active sites.[16,20,23] In fact, the detailed correlation between defects and catalytic properties relies heavily on atomic-level structural identifications. Therefore, developing feasible methods for the manufacture and characterization of defects with atomic-level precision is highly desirable but still challenging.

Moreover, the electrochemical reconstruction of catalysts generally occurs because of high anodic oxidation potentials.[12,21,22] Recently, Fabbri et al. reported that dynamic surface self-reconstruction is the key for electrochemical OER for highly active perovskite-based catalysts.[24] The reconstruction-derived oxy(hydroxide) layers are identified as the true catalytically active sites. As reported, the distinct reconstruction is also observed in many transition-metal dichalcogenides (TMDs), transition-metal oxides (TMOs), and transition-metal hydroxides (TMOH)-based OER/UOR electrocatalysts.[12,16,21] However, understanding the correlation between reconstruction and intrinsic structure is rarely discussed.

Received: March 29, 2018
Accepted: May 17, 2018
Published: May 17, 2018

DOI: 10.1021/acsenergylett.8b00515
ACS Energy Lett. 2018, 3, 1373−1380

In this work, we developed a propylene oxide-mediated alkalinization precipitation method to achieve controllable hydrolysis of Ni^{2+} metal ion aqueous complexes. Various nickel hydroxide (α-$Ni(OH)_2$) samples with adjustable nickel vacancy (V_{Ni}) concentrations (recorded as V_{Ni}-α-$Ni(OH)_2$-x, x = 1, 2, 3, and 4) were successfully prepared. Atomic-level characterization methods, especially X-ray absorption fine structure spectroscopy (XAFS) and positron annihilation spectroscopy (PAS), verified the existence of gradient V_{Ni} concentrations in the obtained samples. Density functional theory (DFT) calculations were conducted to understand the effect of V_{Ni} defects on intrinsic structure and related catalytic performance.

In the experiment, in order to synthesize V_{Ni}-tunable samples, a rate-controlled nucleation and growth process was employed through a controllable hydrolysis procedure (see Experimental Section in the Supporting Information for details), in which the water content played a vital role in the formation of V_{Ni}-rich structures (Figures 1a and S1).[25] A fast hydrolysis rate was achieved in water-less condition, which was revealed by faster pH changes in water-less conditions than that in water-rich conditions (Table S1). The rapid hydrolysis rate resulted in the fast crystal growth process, which contributed to the formation of V_{Ni}.[26] Powder X-ray diffraction (XRD) measurements were first performed to investigate the structural information of these as-prepared samples. Most of these diffraction peaks coincide well with that of previously reported α-$Ni(OH)_2$ samples (Figures 1b and S2).[27,28] Notably, the c-axis plane diffraction peak of V_{Ni}-α-$Ni(OH)_2$-4 obviously shifts to higher degree compared to that of other V_{Ni}-α-$Ni(OH)_2$-x samples, suggesting the reduced interlayer spacing. This result is probably caused by the deficiency of intercalated H_2O molecules in the interlayers.[29] To verify the above conclusion, a β-$Ni(OH)_2$ reference possessing typical brucite-like structure without interlayer H_2O was also synthesized (Figure S3). In high-resolution O 1s X-ray photoelectron spectroscopy (XPS) results, the absence of the H_2O signal peak in V_{Ni}-α-$Ni(OH)_2$-4 and β-$Ni(OH)_2$, together with the presence of H_2O signal peak in V_{Ni}-α-$Ni(OH)_2$-1, supports the deficiency of interlayer H_2O in V_{Ni}-α-$Ni(OH)_2$-4 (Figure S4). This conclusion can be also evidenced by the slightly increased interlayer spacing when a trace amount of water was introduced (Figure S5). Transmission electron microscopy (TEM) images of the obtained V_{Ni}-α-$Ni(OH)_2$-x samples show typical nanosheet-composed structures (Figure S6). A representative, high-resolution TEM (HRTEM) image of the V_{Ni}-α-$Ni(OH)_2$-4 was obtained. As presented in Figure 1c, two continuous and ordered lattice fringes with the same lattice spacing of ~2.31 Å together with the crystal plane angle of 60° are observed, which correspond to the (200) and (020) planes of α-$Ni(OH)_2$, respectively (JCPDS No. 22-0444). This is further confirmed by the corresponding fast Fourier transform (FFT) pattern (the inset in Figure 1c).

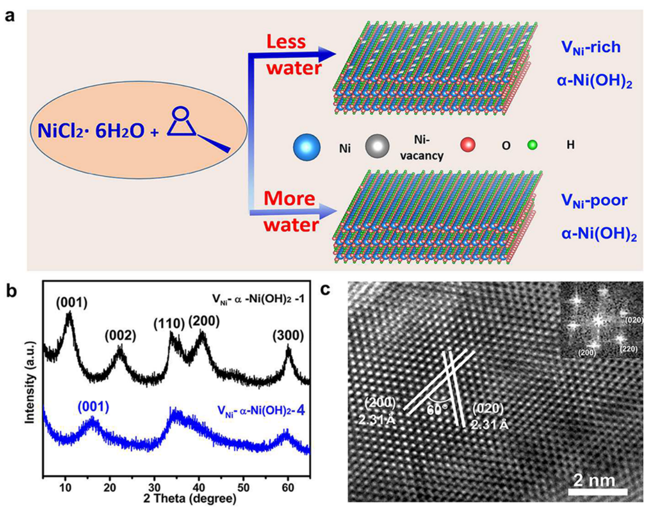

Figure 1. (a) Schematic diagram for the synthesis of V_{Ni}-rich and V_{Ni}-poor α-$Ni(OH)_2$. (b) Typical XRD patterns of V_{Ni}-α-$Ni(OH)_2$-1 and V_{Ni}-α-$Ni(OH)_2$-4. (c) HRTEM image of V_{Ni}-α-$Ni(OH)_2$-4 (Inset: the corresponding FFT pattern).

To further explore the fine structures, advanced spectroscopic techniques were employed to characterize these V_{Ni}-α-$Ni(OH)_2$-x and β-$Ni(OH)_2$ samples. Synchrotron-based XAFS, as one of the most powerful techniques to probe the local atomic structures, was employed.[30−32] As shown in Figure 2a, the Ni K-edge spectra of all the V_{Ni}-α-$Ni(OH)_2$-x samples are similar. Additionally, no energy shift in the amplified spectral features (site A) indicates the existence of a standard α-$Ni(OH)_2$ framework in all samples (Figure 2b), which is consistent with the above XRD results.[12] Notably, positive energy shifts from V_{Ni}-α-$Ni(OH)_2$-1 to V_{Ni}-α-$Ni(OH)_2$-4 occur at the XAFS adsorption edge, suggesting gradually increased average valence state in V_{Ni}-α-$Ni(OH)_2$-x (Figure 2c). Furthermore, the oscillation function curves of V_{Ni}-α-$Ni(OH)_2$-x at the k range of 2−14 $Å^{-1}$ show the consistency, with the exception of the gradually reduced oscillation amplitude (Figure 2d). This suggests the same main structure for all V_{Ni}-α-$Ni(OH)_2$-x samples, with the difference in coordination surrounding the centered Ni atoms (Figure 2d).[20] To obtain direct observations, extended XAFS (EXAFS) was obtained by the Fourier transformation (FT) from the above XAFS data. As can be seen in Figure 2e, there are two main peaks at ~1.56 and ~2.68 Å for all samples, corresponding to the nearest Ni−O and Ni−Ni bonds from the first and second shells, respectively.[33] For comparison, the XAFS results of β-$Ni(OH)_2$ were also analyzed. The larger peak positions for Ni−O (at ~1.62 Å) and Ni−Ni (at ~2.75 Å) in β-$Ni(OH)_2$ are observed and further verify the typical α-$Ni(OH)_2$ phase of the obtained V_{Ni}-α-$Ni(OH)_2$-x (Figure S7). It is worth noting that the intensities of the Ni−Ni peaks follow the sequence of α-$Ni(OH)_2$-1 > V_{Ni}-α-$Ni(OH)_2$-2 > V_{Ni}-α-$Ni(OH)_2$-3 > V_{Ni}-α-$Ni(OH)_2$-4, suggesting generally reduced coordination number (CN); meanwhile, the V_{Ni} exists with gradually increasing concentrations. A recent report has demonstrated that the V_{Ni} would lead to the existence of Ni^{3+} in Ni-based oxide materials.[21] Therefore, the gradually reduced CN and increased valence state revealed by XAFS demonstrate the mounting V_{Ni} in V_{Ni}-α-$Ni(OH)_2$-x.

XPS was used to further confirm the presence of V_{Ni} and qualitatively prove the V_{Ni} concentrations in V_{Ni}-α-$Ni(OH)_2$-x. Except for the peaks assigned to the Ni and O elements, the peaks assigned to the interlayer/absorbed Cl are also observed, implying the hydrotalcite-like structure with partly isomorphous replacement of bivalent metal cations (Ni^{2+}) by the trivalent metal cations (Ni^{3+}) (Figure S8a). To further verify the existence of Ni^{3+}, the high-resolution Ni 2p spectra of all the samples were analyzed. For the β-$Ni(OH)_2$, two characteristic peaks at 855.37 and 873.00 eV assigned to the $2p_{3/2}$ and $2p_{1/2}$ signals of Ni^{2+} are observed (Figure S8b), revealing its typical brucite-like structure without the replacement of Ni^{3+}.

DOI: 10.1021/acsenergylett.8b00515
ACS Energy Lett. 2018, 3, 1373−1380

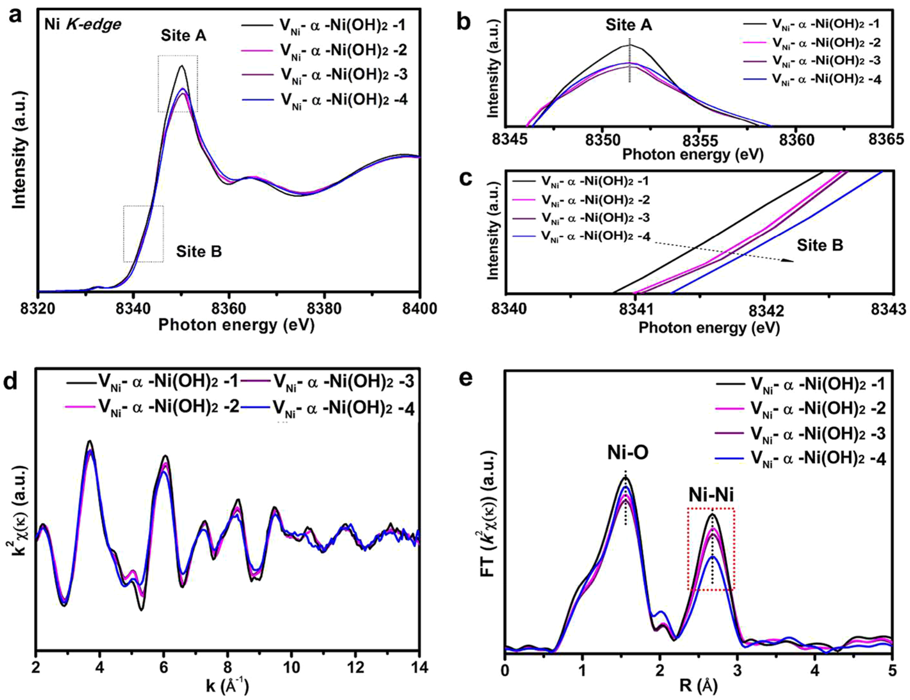

Figure 2. (a) Ni K-edge XAFS curves. (b and c) The magnification of site A (b) and site B (c) in panel a for easy viewing. (d) Corresponding oscillation functions $\kappa^2\chi(k)$ for V_{Ni}-α-Ni(OH)$_2$-x samples. (e) Fourier transformed results of V_{Ni}-α-Ni(OH)$_2$-x samples.

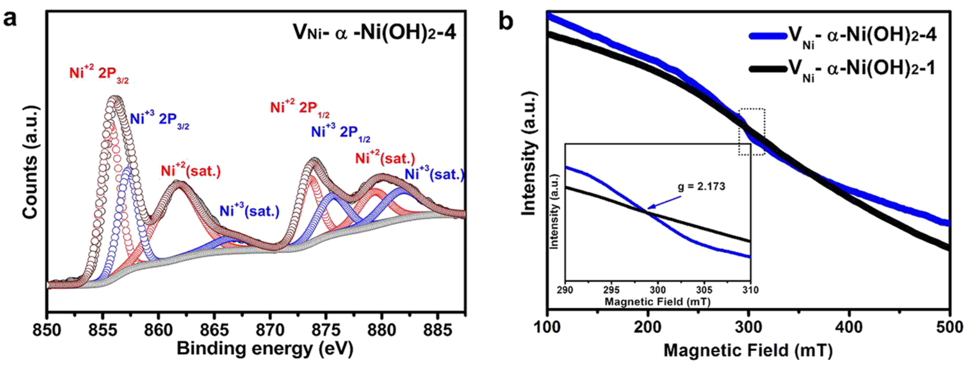

Figure 3. (a) XPS spectrum of Ni 2p for V_{Ni}-α-Ni(OH)$_2$-4. (b) Comparison of ESR results for V_{Ni}-α-Ni(OH)$_2$-4 and V_{Ni}-α-Ni(OH)$_2$-1.

Table 1. Positron Lifetime Parameters of V_{Ni}-α-Ni(OH)$_2$-x Samples Measured at Room Temperature with ^{22}Na as Radioactive Source

samples	τ_1 (ps)	τ_2 (ps)	τ_3 (ns)	I_1 (%)	I_2 (%)	I_3 (%)	I_1/I_2
V_{Ni}-α-Ni(OH)$_2$-1	297.1	415.2	5.34	42.51	56.92	0.57	0.747
V_{Ni}-α-Ni(OH)$_2$-2	301.4	433.0	5.05	74.56	24.94	0.50	2.990
V_{Ni}-α-Ni(OH)$_2$-3	300.7	425.9	4.88	76.01	23.51	0.48	3.233
V_{Ni}-α-Ni(OH)$_2$-4	308.0	432.1	5.17	85.10	14.35	0.55	5.930

As for V_{Ni}-α-Ni(OH)$_2$-x, the results of the Ni 2p XPS spectra indicate that the peaks at 857.35 and 875.70 eV assigned to signals of Ni^{3+} also exist together with the new satellite peaks at high binding energies, besides the contribution of Ni^{2+} (Figures 3a and S8c-e). Thus, the intense and distinct signals of Ni^{3+} in various V_{Ni}-α-Ni(OH)$_2$-x samples imply the existence of considerable V_{Ni}.[21,34] Notably, the V_{Ni}-α-Ni(OH)$_2$-4 shows Ni^{3+} signals that are more intense than those of other V_{Ni}-α-Ni(OH)$_2$-x samples, suggesting the presence of V_{Ni} with the highest concentration in V_{Ni}-α-Ni(OH)$_2$-4. Representatively, the high-concentration V_{Ni} in the V_{Ni}-α-Ni(OH)$_2$-4 was further resolved by electron spin resonance (ESR) measurements. It is shown that the putative Ni^{3+} signal in the ESR spectrum for V_{Ni}-α-Ni(OH)$_2$-4 was observed, while similar or relatively low ESR intensities for V_{Ni}-Fe-α-Ni(OH)$_2$-4 or other V_{Ni}-α-Ni(OH)$_2$-x samples were observed (Figures 3b and S9 and Table S2).[21,35] The ESR analyses further demonstrated the V_{Ni} difference existing in these V_{Ni}-α-Ni(OH)$_2$-x samples.

To obtain the quantification information on defects in the obtained V_{Ni}-α-Ni(OH)$_2$-x samples, PAS measurements, a tool for examining defect types and concentrations, were carried out.[36] As can be seen in Table 1, all samples displayed three distinct lifetime components (τ_1, τ_2, and τ_3) with relative intensities I_1, I_2, and I_3. The two longest lifetimes, τ_2 and τ_3,

DOI: 10.1021/acsenergylett.8b00515
ACS Energy Lett. 2018, 3, 1373−1380

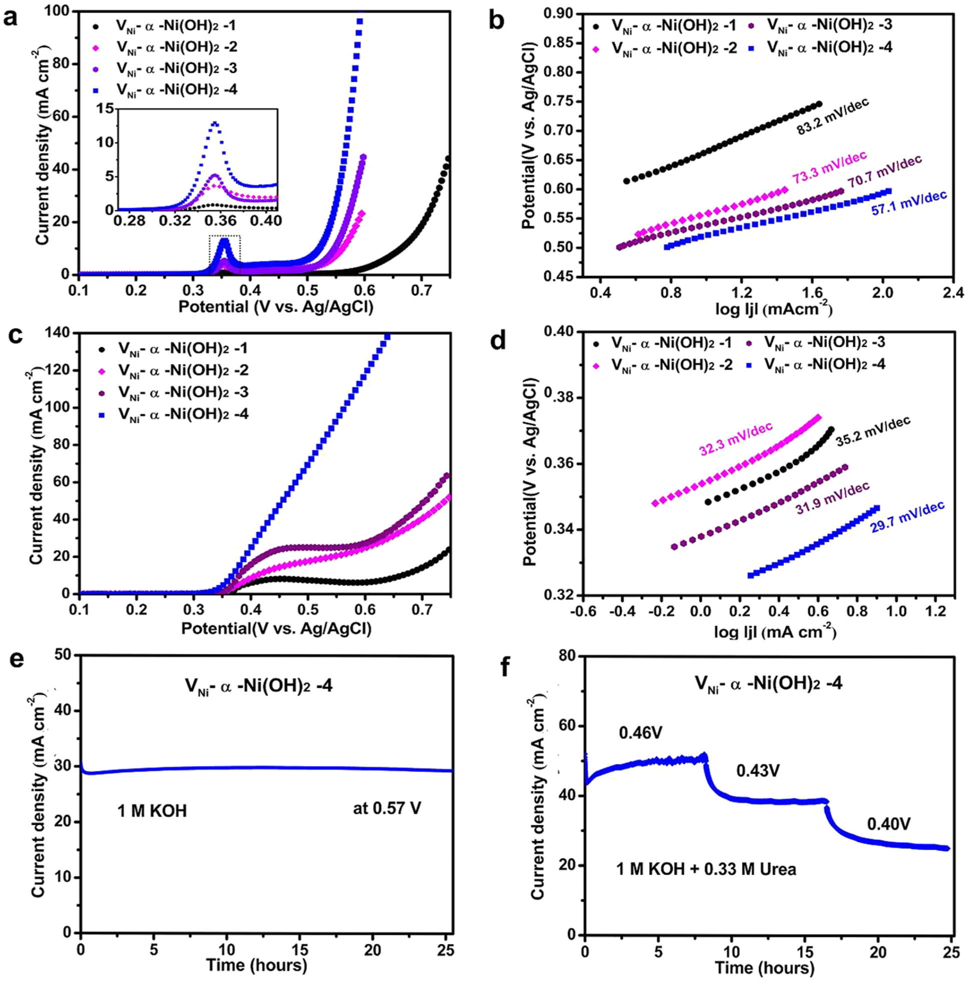

Figure 4. (a) LSV curves and (b) corresponding Tafel slopes for V_{Ni}-α-$Ni(OH)_2$-x samples in 1.0 M KOH electrolyte solution. (c) LSV curves and (d) calculated Tafel slopes for UOR in 1.0 M KOH with the presence of 0.33 M urea. (e and f) Long-term tests for OER and UOR at the given potentials.

could be attributed to the large defect clusters and the interface (or large voids) formed in the samples, respectively.[37,38] The shortest one (τ_1) was assigned to positron annihilation as trapped by V_{Ni}. Moreover, the intensities of positron lifetimes could provide information on the relative defect concentrations. It is noteworthy that I_1 of the V_{Ni}-α-$Ni(OH)_2$-4 reached the highest value (85.10%), which revealed its highest V_{Ni} concentration among these V_{Ni}-α-$Ni(OH)_2$-x samples. The above PAS analyses further confirmed the presence of V_{Ni} and the defect level with the sequence V_{Ni}-α-$Ni(OH)_2$-4 > V_{Ni}-α-$Ni(OH)_2$-3 > V_{Ni}-α-$Ni(OH)_2$-2 > V_{Ni}-α-$Ni(OH)_2$-1.

As reported, $Ni(OH)_2$-based materials can serve as efficient OER and UOR catalysts.[12,39] Figure 4a shows the OER linear scan voltammetry (LSV) curves of V_{Ni}-α-$Ni(OH)_2$-x in 1.0 M KOH solution. Obviously, the V_{Ni}-α-$Ni(OH)_2$-4 achieved a current density of 10 mA cm^{-2} at 0.515 V versus Ag/AgCl, which is lower than that of V_{Ni}-α-$Ni(OH)_2$-3 (0.547 V), V_{Ni}-α-$Ni(OH)_2$-2 (0.561 V), V_{Ni}-α-$Ni(OH)_2$-1 (0.664 V), and IrO_2 (0.530 V) (Table S3 and Figure S10a). This result demonstrates the positive correlation between OER activities and V_{Ni} concentrations, implying the key role of the V_{Ni} in OER. The superior catalytic activities of V_{Ni}-α-$Ni(OH)_2$-4 catalyst was also demonstrated by the smallest Tafel slope of 57.1 mV $decade^{-1}$ among all V_{Ni}-α-$Ni(OH)_2$-x catalysts, which was even comparable to that of IrO_2 (Figures 4b and S10b). To further investigate the charge-transfer abilities, the electrochemical impedance spectroscopy (EIS) measurements were carried out. The obtained Nyquist plots of V_{Ni}-α-$Ni(OH)_2$-x samples exhibited gradually decreased charge-transfer resistance (R_{ct}) with increasing V_{Ni} (Figure S11), revealing continuously promoted charge-transfer abilities in these catalysts. To access the intrinsic activities of active sites in the above materials for OER, it is assumed that all metallic Ni sites were catalytically active, and the turnover frequencies (TOFs) are calculated (Figure S12). Apparently, the V_{Ni}-α-$Ni(OH)_2$-4 catalyst shows a high TOF value (0.156 s^{-1}) at a potential of 0.59 V versus Ag/AgCl, which is approximately 2.4, 4.3, and 52.0 times higher than that of V_{Ni}-α-$Ni(OH)_2$-3 (0.064 s^{-1}), V_{Ni}-α-$Ni(OH)_2$-2 (0.036 s^{-1}), and V_{Ni}-α-$Ni(OH)_2$-1 (0.003 s^{-1}), respectively. To further exclude the effect of the active surface areas, the roughness factors (R_f) are calculated from cyclic voltammetry (CV) curves in the double-layer regions by assuming the value of 60 μF cm^{-2} for the capacitance of a smooth surface.[40] It is obvious that these V_{Ni}-α-$Ni(OH)_2$-x catalysts show the increasing intrinsic current density (true value) and reduced potential with increasing V_{Ni} concentration (Figure S13 and Table S3). The above OER analyses indicated that the catalysts with higher V_{Ni} concentration delivered faster charge transfer and more favorable reaction kinetics, thereby realizing more active OER than those with lower V_{Ni} concentration. As

DOI: 10.1021/acsenergylett.8b00515
ACS Energy Lett. 2018, 3, 1373−1380

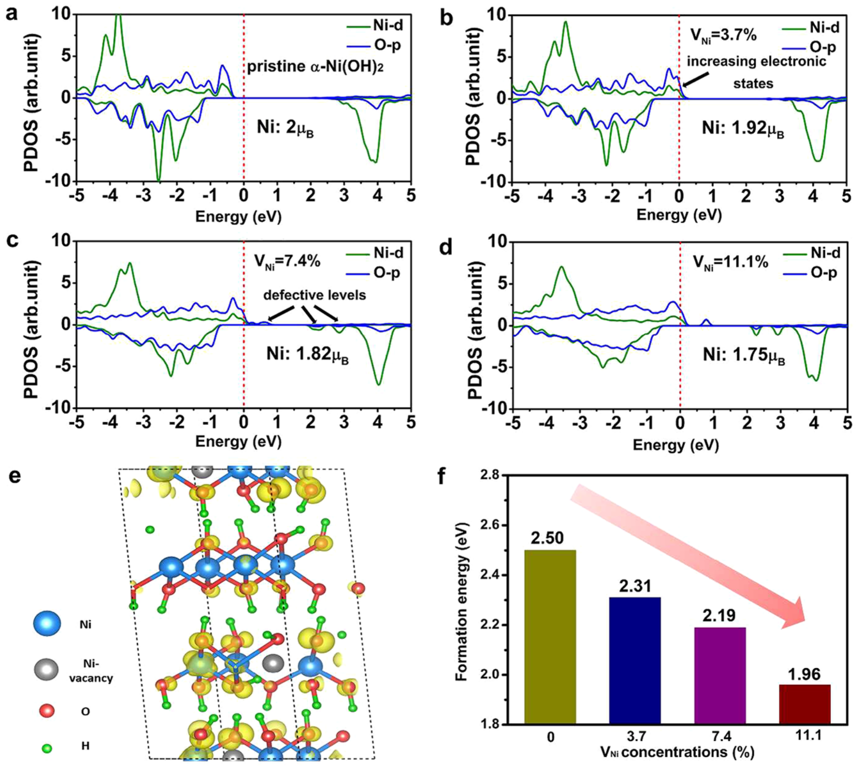

Figure 5. (a–d) DFT-based DOS spectra of α-Ni(OH)$_2$ with V$_{Ni}$ concentrations of 0, 3.7%, 7.4%, and 11.1%, respectively. The red dashed line is the Fermi level set to zero. (e) The simulated distribution of partial charge density at the Fermi level induced by V$_{Ni}$ incorporation. (f) The calculated formation energies for γ-NiOOH from α-Ni(OH)$_2$ with different V$_{Ni}$ concentrations.

reported, Fe incorporation in Ni-based OER catalysts can efficiently promote the electrochemical activity.[41,42] To exclude the presence of trace Fe in sample preparation procedure and further promote the OER activity, a Fe-doped V$_{Ni}$-α-Ni(OH)$_2$-4 sample (V$_{Ni}$-Fe-α-Ni(OH)$_2$-4) was prepared. Inductively coupled plasma-mass spectrometry (ICP-MS) measurements were carried out to evaluate the distribution of Ni and Fe. The ICP-MS results demonstrate the absence of Fe in V$_{Ni}$-α-Ni(OH)$_2$-4, while a small amount of Fe (~4.6 atom %) is obtained in V$_{Ni}$-Fe-α-Ni(OH)$_2$-4 (Table S4). The electrochemical measurements demonstrate that Fe incorporation can significantly boost the OER activities (Figure S14). The catalytic performance of samples for UOR in 1.0 M KOH with the presence of 0.33 M urea was also evaluated. Similar to the above OER catalytic performance, enhanced oxidation current densities and reduced onset potentials were also achieved with increasing V$_{Ni}$, as revealed by the polarization curves (Figure 4c). Furthermore, the calculated Tafel slopes suggested that the V$_{Ni}$-α-Ni(OH)$_2$-4 catalyst achieved faster reaction kinetics compared to other V$_{Ni}$-α-Ni(OH)$_2$-x and Pt/C catalysts (Figures 4d and S15). Similarly, the obtained charge-transfer resistance and TOFs also revealed the better catalytic activity of the catalyst with higher V$_{Ni}$ concentration (Figure S16 and Table S5). Long-term stability, one very important criterion in judging electrochemical performance, is necessary for electrode materials. To probe the durability of the electrocatalysts, the chronoamperometry measurements were performed over 20 h under the given potentials. It is noteworthy that the current densities showed negligible declines in both OER and UOR catalytic processes, suggesting the excellent catalytic stability (Figures 4e,f and S17).

In the above OER and UOR catalytic measurements, the catalyst with high V$_{Ni}$ concentration showed boosted catalytic performance. To shed light on the origin of this result, the catalytic process and related intrinsic mechanism were explored. According to considerable previous contributions, the electrochemical oxidation of Ni^{2+} to Ni^{3+} species (typical NiOOH) in its oxides/hydroxides catalysts is reversible and determines the OER and UOR rates in the electrochemical processes.[12,21] Therefore, we further explored the correlation between reactive species formation and defective structures. In these V$_{Ni}$-α-Ni(OH)$_2$-x catalysts, the distinct oxidation peaks (Ni^{2+}/Ni^{3+}) at ~0.355 V versus Ag/AgCl were observed (the inset of Figure 4a), suggesting the similar reconstruction phenomenon. Interestingly, the V$_{Ni}$-α-Ni(OH)$_2$-x with higher V$_{Ni}$ concentration displays stronger oxidation peaks, implying the easier formation of active species. This further demonstrates that the V$_{Ni}$ in V$_{Ni}$-α-Ni(OH)$_2$-x plays a vital role in the formation of active species from reconstruction. Subsequently, the larger current densities were achieved in the catalysts with higher V$_{Ni}$ concentrations. To further explore the reconstruction, the XPS results of the catalyst after the electrochemical tests were compared with that of the fresh catalyst before the tests. In Ni 2p XPS spectra, the binding energy in V$_{Ni}$-α-Ni(OH)$_2$-4 shows a more positive shift relative to that in V$_{Ni}$-α-Ni(OH)$_2$-1, further demonstrating the much reconstruction in V$_{Ni}$-α-Ni(OH)$_2$-4 with high V$_{Ni}$ concentration (Figure S18a,b). This conclusion was also verified by the existence of distinct O^{2-} species assigned to the NiOOH (Figure S18c,d).

To understand the roles of V$_{Ni}$ and its concentrations on the electronic structures, DFT calculations were performed. First, the density of states (DOS) of pristine α-Ni(OH)$_2$ and V$_{Ni}$-defective α-Ni(OH)$_2$ were analyzed. As shown in Figure 5a,b,

DOI: 10.1021/acsenergylett.8b00515
ACS Energy Lett. 2018, 3, 1373–1380

the defective α-Ni(OH)$_2$ with V_{Ni} concentration of 3.7% exhibited higher DOS near the Fermi level compared to the pristine α-Ni(OH)$_2$. The increased DOS would accelerate the charge-transfer process to facilitate the reconstruction, thereby obtaining the active species (NiOOH).[12,21] Furthermore, the DOS of defective α-Ni(OH)$_2$ with high defect concentrations of 7.4% and 11.1% were considered. As displayed in Figure 5c,d, a continuous enhancement of DOS near the Fermi level could be obtained with the increase of V_{Ni} concentrations, suggesting the increased electronic conductivity for accelerated charge transfer. This was further illustrated by the calculated distribution of partial charge density at the Fermi level upon V_{Ni} introduction (Figure 5e). Meanwhile, a consecutive reduction of Bohr magneton from 2 μ_B to 1.75 μ_B was also realized, and this reduction could represent the decreased electron spin filling of e_g orbitals. The decreased e_g occupancy would enhance the metal−oxygen bond strength, thus leading to enhanced catalytic activities.[16,21,43] Notably, one can see that the V_{Ni}-rich α-Ni(OH)$_2$ with high defect concentrations exhibits new defect levels in the band gap. The appearance of defect levels means improved carrier density, thereby enhancing charge transport properties of catalysts.[36,44] In brief, the presence of V_{Ni} leads to the appearance of new defect levels and the increase of hole density near the Fermi level, which can accelerate the charge transfer to facilitate the formation of active species.

As reported, α-Ni(OH)$_2$ would be reassembled and transformed to γ-NiOOH as active species in the electrochemical OER process.[39] To further comprehend the vital roles of V_{Ni} in the formation of active species, theoretical formation energies of active γ-NiOOH from the initial α-Ni(OH)$_2$ with different V_{Ni} concentrations were also calculated (see computational details in Experimental Section). As can be seen in Figure 5f, the calculated formation energies were gradually reduced with increasing V_{Ni} concentration, further suggesting the positive role of V_{Ni} introduction. In detail, the α-Ni(OH)$_2$ with the highest V_{Ni} concentration of 11.1% displayed the lowest formation energy of 1.96 eV, which was much less than the pristine one (2.50 eV). As a direct outcome, V_{Ni}-defective α-Ni(OH)$_2$ samples exhibit superior electrocatalytic activities with increasing V_{Ni}.

In conclusion, we have successfully developed efficient α-Ni(OH)$_2$ electrocatalysts with tunable Ni vacancies and provided novel understanding of vacancy-promoted reconstruction during anodic oxidation reactions. The detailed electrochemical measurements suggested that the α-Ni(OH)$_2$ catalysts could show improved activities with the increasing V_{Ni} concentrations. Based on the experimental data, DFT simulations revealed that the introduction of V_{Ni} could enhance the intrinsic conductivities of α-Ni(OH)$_2$ catalysts, thereby boosting the formation of active species to promote electrochemical oxidation processes. This study demonstrates that defect-engineered strategies and atomic-level spectroscopic characterization combined with theoretical calculations provide in-depth understanding of structure−property relationships for electrocatalysts. The concept demonstrated here calls for future efforts toward atomic defect engineering in electrocatalyst design.

■ ASSOCIATED CONTENT

Supporting Information

The Supporting Information is available free of charge on the ACS Publications website at DOI: 10.1021/acsenergylett.8b00515.

> Experimental Section; Figure S1 showing the diagram of synthesis and photos of reaction procedure at different times; Figures S2, S3, S5, and S6 showing XRD, TEM, and HRTEM results of different samples; Figures S4, S8, and S18 showing XPS results of different samples; Figure S7 showing the XAFS data for different materials; Figure S9 showing the ESR results; Figures S10−S17 showing electrochemical results of these samples; Tables S1−S3 exhibiting the pH values of reaction solvents at different times, ESR details, ICP-MS results, and activity comparison (PDF)

■ AUTHOR INFORMATION

Corresponding Authors

*E-mail: jhlworld@ustc.edu.cn.
*E-mail: xjwu@ustc.edu.cn.
*E-mail: song2012@ustc.edu.cn.

ORCID

Hongliang Jiang: 0000-0002-5243-3524
Xiaojun Wu: 0000-0003-3606-1211
Li Song: 0000-0003-0585-8519

Author Contributions

§Q.H. and Y.W. contributed equally to this work. L.S. and H.J. planned the project. Q.H. carried out most of the sample preparation and material measurement. Y.W. and X.W. performed DFT calculations. Z.P., M.W., and B.Y. conducted PAS experiments and data analysis. C.W. helped to carry out XAFS experiments. P.M.A. and other authors discussed the results and participated in writing the manuscript.

Notes

The authors declare no competing financial interest.

■ ACKNOWLEDGMENTS

This work is financially supported by Ministry of Science and Technology of the People's Republic of China (MOST, 2014CB848900, 2016YFA0200602, 2017YFA0303500), National Natural Science Foundation of China (NSFC, U1532112, 11375198, 11574280, 21573204, 21706248, and 21421063), CAS Interdisciplinary Innovation Team, and Key Laboratory of Advanced Energy Materials Chemistry (Ministry of Education) in Nankai University (111 project, B12015). We thank the Shanghai synchrotron Radiation Facility (14W1, SSRF), the Beijing Synchrotron Radiation Facility (1W1B and soft-X-ray endstation, BSRF), and the Hefei Synchrotron Radiation Facility (Photoemission, MCD and ARPES Endstations, NSRL). We acknowledge Dr. Shuangming Chen for his help in XAFS analysis.

■ REFERENCES

(1) Dou, S.; Tao, L.; Huo, J.; Wang, S. Y.; Dai, L. M. Etched and Doped Co_9S_8/Graphene Hybrid for Oxygen Electrocatalysis. *Energy Environ. Sci.* **2016**, *9*, 1320−1326.

(2) Armand, M.; Tarascon, J. M. Building Better Batteries. *Nature* **2008**, *451*, 652−657.

DOI: 10.1021/acsenergylett.8b00515
ACS Energy Lett. 2018, 3, 1373−1380

(3) Gong, K. P.; Du, F.; Xia, Z. H.; Durstock, M.; Dai, L. M. Nitrogen-Doped Carbon Nanotube Arrays with High Electrocatalytic Activity for Oxygen Reduction. *Science* **2009**, *323*, 760−764.
(4) Song, Z.; Schenk, K.; Hu, X. L. A Nanoporous Oxygen Evolution Catalyst Synthesized by Selective Electrochemical Etching of Perovskite Hydroxide $CoSn(OH)_6$ Nanocubes. *Energy Environ. Sci.* **2016**, *9*, 473−477.
(5) Zhang, G.; Wang, G. H.; Liu, Y.; Liu, H. J.; Qu, J. H.; Li, J. H. Highly Active and Stable Catalysts of Phytic Acid-Derivative Transition Metal Phosphides for Full Water Splitting. *J. Am. Chem. Soc.* **2016**, *138*, 14686−14693.
(6) Ma, T. Y.; Dai, S.; Jaroniec, M.; Qiao, S. Z. Metal-Organic Frameworks Derived Hybrid Co_3O_4-Carbon Porous Nanowire Arrays as Reversible Oxygen Evolution Electrodes. *J. Am. Chem. Soc.* **2014**, *136*, 13925−13931.
(7) Guo, F.; Ye, K.; Du, M.; Huang, X. M.; Cheng, K.; Wang, G. L. Electrochemical Impedance Analysis of Urea Electro-Oxidation Mechanism on Nickel Catalyst in Alkaline Medium. Electrochim. *Electrochim. Acta* **2016**, *210*, 474−482.
(8) Bergmann, A.; Moreno, E. M.; Teschner, D.; Chernev, P.; Gliech, M.; Araujo, J. F.; Reier, T.; Dau, H.; Strasser, P. Reversible Amorphization and the Catalytically Active State of Crystalline Co_3O_4 During Oxygen Evolution. *Nat. Commun.* **2015**, *6*, 8625.
(9) Zhang, B.; Zheng, X. L.; Voznyy, O.; Comin, R.; Bajdich, M.; Melchor, M. G.; Han, L. L.; Xu, J. X.; Liu, M.; Zheng, L. R.; et al. Homogeneously Dispersed, Multimetal Oxygen-Evolving Catalysts. *Science* **2016**, *352*, 333−337.
(10) Grimaud, A.; Moralrs, O. D.; Han, B. H.; Hong, W. T.; Lee, Y.-L.; Giordano, L.; Stoerzinger, K. A.; Koper, M. T. M.; Yang, S.-H. Activating Lattice Oxygen Redox Reactions in Metal Oxides to Catalyze Oxygen Evolution. *Nat. Chem.* **2017**, *9*, 457−465.
(11) Chen, P. Z.; Xu, K.; Fang, Z. W.; Tong, Y.; Lu, X. L.; Peng, X.; Ding, H.; Wu, C. Z.; Xie, Y. Metallic Co_4N Porous Nanowire Arrays Activated by Surface Oxidation as Electrocatalysts for the Oxygen Evolution Reaction. *Angew. Chem., Int. Ed.* **2015**, *54*, 14710−14714.
(12) Zhu, X. J.; Dou, X. Y.; Dai, J.; An, X. D.; Guo, Y. Q.; Zhang, L. D.; Tao, S.; Zhao, J. Y.; Chu, W. S.; Zeng, X. C.; et al. Metallic Nickel Hydroxide Nanosheets Give Superior Electrocatalytic Oxidation of Urea for Fuel Cells. *Angew. Chem., Int. Ed.* **2016**, *55*, 12465−12469.
(13) Chen, S.; Duan, J. J.; Vasileff, A.; Qiao, S. Z. Size Fractionation of Two-Dimensional Sub-Nanometer Thin Manganese Dioxide Crystals towards Superior Urea Electrocatalytic Conversion. *Angew. Chem., Int. Ed.* **2016**, *55*, 3804−3808.
(14) Nong, H. N.; Oh, H.-S.; Reier, T.; Willinger, E.; Willinger, M.-G.; Petkov, V.; Teschner, D.; Strasser, P. Oxide-Supported IrNiOx Core-Shell Particles as Efficient, Cost-Effective, and Stable Catalysts for Electrochemical Water Splitting. *Angew. Chem., Int. Ed.* **2015**, *54*, 2975−2979.
(15) Liu, P. F.; Yang, S.; Zheng, L. R.; Zhang, B.; Yang, H. G. Mo^{6+} Activated Multimetal Oxygen-Evolving Catalyst. *Chem. Sci.* **2017**, *8*, 3484−3488.
(16) Liu, Y. W.; Cheng, H.; Lyu, M. J.; Fan, S. J.; Liu, Q. H.; Zhang, W. S.; Zhi, Y. D.; Wang, C. M.; Xiao, C.; Wei, S. Q.; et al. Low Overpotential in Vacancy-Rich Ultrathin $CoSe_2$ Nanosheets for Water Oxidation. *J. Am. Chem. Soc.* **2014**, *136*, 15670−15675.
(17) Liu, Y. W.; Xiao, C.; Li, Z.; Xie, Y. Vacancy Engineering for Tuning Electron and Phonon Structures of Two-Dimensional Materials. *Adv. Energy Mater.* **2016**, *6*, 1600436.
(18) Zhuang, L. Z.; Ge, L.; Yang, Y. S.; Li, M. R.; Jia, Y.; Yao, X. D.; Zhu, Z. H. Ultrathin Iron-Cobalt Oxides Nanosheets with Abundant Oxygen Vacancies for the Oxygen Evolution Reaction. *Adv. Mater.* **2017**, *29*, 1606793.
(19) Wang, H.; Zhang, J. J.; Hang, X. D.; Zhang, X. D.; Xie, J. F.; Pan, B. C.; Xie, Y. Half-Metallicity in Single-Layered Manganese Dioxide Nanosheets by Defect Engineering. *Angew. Chem., Int. Ed.* **2015**, *54*, 1195−1199.
(20) Wang, Y. Y.; Zhang, Y. Q.; Liu, Z. J.; Xie, C.; Feng, S.; Liu, D. D.; Shao, M. F.; Wang, S. Y. Layered Double Hydroxide Nanosheets with Multiple Vacancies Obtained by Dry Exfoliation as Highly Efficient Oxygen Evolution Electrocatalysts. *Angew. Chem., Int. Ed.* **2017**, *56*, 5867−5871.
(21) Zhao, Y. F.; Jia, X. D.; Chen, G. B.; Shang, L.; Waterhouse, G. I. N.; Wu, L.-Z.; Tung, C.-H.; O'Hare, D.; Zhang, T. R. Ultrafine NiO Nanosheets Stabilized by TiO_2 from Monolayer NiTi-LDH Precursors: An Active Water Oxidation Electrocatalyst. *J. Am. Chem. Soc.* **2016**, *138*, 6517−6524.
(22) Xie, J. F.; Zhang, X. D.; Zhang, H.; Zhang, J. J.; Li, S.; Wang, R. X.; Pan, B. C.; Xie, Y. Intralayered Ostward Ripening to Ultrathin Nanomesh Catalyst with Robust Oxygen-Evolving Performance. *Adv. Mater.* **2017**, *29*, 1604765.
(23) Liu, R.; Wang, Y. Y.; Liu, D. D.; Zou, Y. Q.; Wang, S. Y. Water-Plasma-Enabled Exfoliation of Ultrathin Layered Double Hydroxide Nanosheets with Multivacancies for Water Oxidation. *Adv. Mater.* **2017**, *29*, 1701546.
(24) Fabbri, E.; Nachtegaal, M.; Binninger, T.; Cheng, X.; Kim, B.-J.; Durst, J.; Bozza, F.; Graule, T.; Schaublin, R.; Wiles, L.; et al. Dynamic Surface Self-Reconstruction is the Key of Highly Active Perovskite Nano-Electrocatalysts for Water Splitting. *Nat. Mater.* **2017**, *16*, 925−931.
(25) Tarutani, N.; Tokudome, Y.; Jobbagy, M.; Viva, F. A.; S-Illia, G. J. A. A.; Takahashi, M. Single-Nanometer-Sized Low-Valence Metal Hydroxide Crystals: Synthesis via Epoxide-Mediated Alkalinization and Assembly toward Functional Mesoporous Materials. *Chem. Mater.* **2016**, *28*, 5606−5610.
(26) Fang, Z. L.; Bueken, B.; Vos, D. E. D.; Fischer, R. A. Defect-Engineered Metal-Organic Frameworks. *Angew. Chem., Int. Ed.* **2015**, *54*, 7234−7254.
(27) Meng, X. H.; Deng, D. Bio-Inspired Synthesis of α-$Ni(OH)_2$ Nanobristles on Various Substrates and Their Applications. *J. Mater. Chem. A* **2016**, *4*, 6919−6925.
(28) Liang, J.; Dong, B. T.; Ding, S. J.; Li, C. P.; Li, B. Q.; Li, J.; Yang, G. Facile Construction of Ultrathin Standing α-$Ni(OH)_2$ Nanosheets on Halloysite Nanotubes and Their Enhanced Electrochemical Capacitance. *J. Mater. Chem. A* **2014**, *2*, 11299−11304.
(29) Liu, P. F.; Li, X.; Yang, S.; Zu, M. Y.; Liu, P. R.; Zhang, B.; Zheng, L. R.; Zhao, H. J.; Yang, H. G. $Ni_2P(O)/Fe_2P(O)$ Interface Can Boost Oxygen Evolution Electrocatalysis. *ACS Energy Lett.* **2017**, *2*, 2257−2263.
(30) Lai, Q. X.; Zheng, L. R.; Liang, Y. Y.; He, J. P.; Zhao, J. X.; Chen, J. H. Metal-Organic-Framework-Derived Fe-N/C Electrocatalyst with Five-Coordinated Fe-N_x Sites for Advanced Oxygen Reduction in Acid Media. *ACS Catal.* **2017**, *7*, 1655−1663.
(31) Mao, J. J.; Chen, W. X.; He, D. S.; Wan, J. W.; Pei, J. J.; Dong, J. C.; Wang, Y.; An, P. F.; Jin, Z.; Xing, W.; et al. Design of Ultrathin Pt-Mo-Ni Nanowire Catalysts for Ethanol Electrooxidation. *Sci. Adv.* **2017**, *3*, e1603068.
(32) Deng, D. H.; Chen, X. Q.; Yu, L.; Wu, X.; Liu, Q. F.; Liu, Y.; Yang, H. X.; Tian, H. F.; Hu, Y. F.; Du, P. P.; et al. A Single Iron Site Confined in a Graphene Matrix for the Catalytic Oxidation of Benzene at Room Temperature. *Sci. Adv.* **2015**, *1*, e1500462.
(33) Zhu, Y. Q.; Cao, C. B.; Tao, S.; Chu, W. S.; Wu, Z. Y.; Li, Y. D. Ultrathin Nickel Hydroxide and Oxide Nanosheets: Synthesis, Characterizations and Excellent Supercapacitor Performances. *Sci. Rep.* **2015**, *4*, 5787.
(34) Fominykh, K.; Feckl, J. M.; Sicklinger, J.; Doblinger, M.; Bocklein, S.; Ziegler, J.; Peter, L.; Rathousky, J.; Scheidt, E.-W.; Bein, T.; et al. Ultrasmall Dispersed Crystalline Nickel Oxide Nanoparticles as High-Performance Catalysts for Electrochemical Water Splitting. *Adv. Funct. Mater.* **2014**, *24*, 3123−3129.
(35) Zhao, Y. F.; Wang, Q.; Bian, T.; Yu, H. J.; Fan, H.; Zhou, C.; Wu, L.-Z.; Tung, C.-H.; O'Hare, D.; Zhang, T. R. Ni^{3+} Doepd Monolayer Layered Double Hydroxide Nanosheets as Efficient Electrodes for Supercapacitors. *Nanoscale* **2015**, *7*, 7168−7173.
(36) Zhao, Y. F.; Chen, G. B.; Bian, T.; Zhou, C.; Waterhouse, G. I. N.; Wu, L.-Z.; Tung, C.-H.; Smith, L. J.; O'Hare, D.; Zhang, T. R. Defect-Rich Ultrathin ZnAl-Layered Double Hydroxide Nanosheets for Efficient Photoreduction of CO_2 to CO with Water. *Adv. Mater.* **2015**, *27*, 7824−7831.

DOI: 10.1021/acsenergylett.8b00515
ACS Energy Lett. 2018, 3, 1373−1380

(37) Liu, Y. W.; Hua, X. M.; Xiao, C.; Zhou, T. F.; Huang, P. C.; Guo, Z. P.; Pan, B. C.; Xie, Y. Heterogeneous Spin State in Ultrathin Nanosheets Induce Subtle Lattice Distortion to Trigger Efficient Hydrogen Evolution. *J. Am. Chem. Soc.* **2016**, *138*, 5087−5092.
(38) Liu, X. W.; Zhou, K. B.; Wang, L.; Wang, B. Y.; Li, Y. D. Oxygen Vacancy Clusters Promoting Reducibility and Activity of Ceria Nanorods. *J. Am. Chem. Soc.* **2009**, *131*, 3140−3141.
(39) Gao, M. R.; Sheng, W. G.; Zhuang, Z. B.; Fang, Q. R.; Gu, S.; Jiang, J.; Yan, Y. S. Efficient Water Oxidation Using Nanostructured α-Nickel-Hydroxide as an Electrocatalyst. *J. Am. Chem. Soc.* **2014**, *136*, 7077−7084.
(40) Cui, B.; Lin, H.; Li, J. B.; Li, X.; Yang, J.; Tao, J. Core-Ring Structured $NiCo_2O_4$ Nanoplatelets: Synthesis, Characterization, and Electrocatalytic Applications. *Adv. Funct. Mater.* **2008**, *18*, 1440−1447.
(41) Burke, M. S.; Zou, S.; Enman, L. J.; Kellon, J. E.; Gabor, C. A.; Pledger, E.; Boettcher, S. W. Revised Oxygen Evolution Reaction Activity Trends for First-Row Transition-Metal (Oxy)hydroxides in Alkaline Media. *J. Phys. Chem. Lett.* **2015**, *6*, 3737−3742.
(42) Burke, M. S.; Kast, M. G.; Trotochaud, L.; Smith, A. M.; Boettcher, S. W. Cobalt-iron (Oxy)hydroxide Oxygen Evolution Electrocatalysts: The Role of Structure and Composition on Activity, Stability, and Mechanism. *J. Am. Chem. Soc.* **2015**, *137*, 3638−3648.
(43) Liu, Y. W.; Xiao, C.; Lyu, M. J.; Lin, Y.; Cai, W. Z.; Huang, P. C.; Tong, W.; Zou, Y. M.; Xie, Y. Ultrathin Co_3S_4 Nanosheets that Synergistically Engineer Spin States and Exposed Polyhedra that Promote Water Oxidation under Neutral Conditions. *Angew. Chem., Int. Ed.* **2015**, *54*, 11231−11235.
(44) Gao, S.; Jiao, X. C.; Sun, Z. T.; Zhang, W. H.; Sun, Y. F.; Wang, C. M.; Hu, Q. T.; Zu, X. L.; Yang, F.; Yang, S. Y.; et al. Ultrathin Co_3O_4 Layers Realizing Optimized CO_2 Electroreduction to Formate. *Angew. Chem., Int. Ed.* **2016**, *55*, 698−702.

DOI: 10.1021/acsenergylett.8b00515
ACS Energy Lett. 2018, 3, 1373−1380